Unconventional Surface Charging within Deep Cavities on Airless Planetary Bodies: Particle-in-Cell Plasma Simulations

J. Nakazono[1], Y. Miyake[1]

[1]Graduate School of System Informatics, Kobe University, 1-1, Rokkodai-cho, Nada-ku, Kobe 657-8501, Japan.

Key Points:

- Unconventional current ordering between solar wind ion and electron is established at the bottom of deep cavities on the Moon and asteroids
- Cavity bottom surface could have significant positive potentials that rank with the kinetic energies of solar wind ions
- Photoelectrons no longer promote positive charging by themselves but rather relax the positive potentials at the cavity bottom

Corresponding author: Jin Nakazono, nakazono.jin@stu.kobe-u.ac.jp

Abstract

Surface charging properties of a non-conducting surface that has a deep cavity and is in contact with the solar wind plasma are investigated by means of the particle-in-cell plasma simulations. The modeled topography is intended with a portion of irregular surfaces found on solid planetary bodies. The simulations have revealed unconventional charging features in that the cavity bottom is charged up to positive values even without any electron emission processes such as photoemission, provided that the surface location is accessible to a portion of incoming solar wind ions. The major driver of the positive charging is identified as drifting ions of the solar wind plasma, and an uncommon current ordering where ion currents exceed electron currents is established at the innermost part of the deep cavity. This also implies that the cavity bottom surface may have a positive potential of several hundred volts, corresponding to the kinetic energy of the ions. The present study also clarifies the role of photoelectrons in developing the distinctive charging environment inside the cavity. The photoemitted electrons can no longer trigger positive charging at the cavity bottom, but rather exhibit the effect of relaxing positive potentials caused by the solar wind ions. The identified charging process, which are primarily due to the solar wind ions, are localized at the depths of the cavity and may be one possible scenario for generating intense electric fields inside the cavity.

Plain Language Summary

Model predictions based on the kinetic plasma simulations suggest an unconventional surface electrical charging condition within deep cavities, which can be formed on the Moon and other airless planetary bodies directly impacted by the solar wind. Due to the differentiated directionality of solar wind ion and electron motions, ions are more likely to reach the innermost part of such deep cavities than electrons without being lost at the cavity sidewall. At the bottom of cavities with depth-width aspect ratios above a certain level, the ion current tends to exceed the electron current. The condition leads to significant positive potentials that rank with the kinetic energies of solar wind ions, which is completely independent of the work done by photoelectron emission. The identified positive charging process, which are primarily due to the solar wind ions, are localized at the depths of cavities and may be one possible scenario for strong electric fields on the dayside of the Moon and asteroids.

1 Introduction

A solid surface that is in contact with a plasma collects electric charges of impinging electrons and ions. In general, due to the higher differential influx of electrons than that of ions, the surface gets charged negatively, that is, acquires a negative potential with respect to the environment (Whipple, 1981). This potential field exerts a repulsive force for approaching electrons and restrains further inflow of thermal electrons. The equilibrium (or floating) potential is eventually reached when the positive and negative charge inflows are balanced; i.e., the net current flow into the surface becomes zero. This concept of current balance holds also in the presence of additional current components that are caused by emission processes of charged particles. The charging process (e.g., Garrett, 1981) and its feedback to plasma environment, such as the formation of sheaths and presheaths (e.g., Robertson, 2013; Scheiner et al., 2015), have been investigated extensively. In space applications, the understanding of charging processes has been developed through long-standing studies of spacecraft charging as well as probe measurements (e.g., Garrett & Whittlesey, 2000; Fahleson, 1967).

The surface charging is a significant research area also for the physics of airless, solid planetary bodies in the solar system, such as the Moon and asteroids (Manka, 1973; Stubbs et al., 2014; Zimmerman et al., 2014). This is because charging possibly leads to electrostatic transport of charged dust grains on their surfaces (Nitter et al., 1998; Stubbs,

Vondrak, & Farrell, 2007). Such natural bodies covered with non-conducting regolith layers exhibit manifested differential charging depending on both space-environmental and surface conditions. On-orbit observations and theoretical predictions have shown that the darkside and terminator regions of the Moon have negative surface potentials, whereas the dayside surface has positive potentials (Halekas et al., 2002, 2008; Stubbs, HalekaS, et al., 2007; Farrell et al., 2010). In light of the fact that an ambient plasma by itself tends to make solid surfaces charge negatively, it is acknowledged that the positive equilibrium potentials on the day side are made possible by the aid of negative charge transfer from the surface to space though electron emission processes such as photoemission (e.g., Freeman & Ibrahim, 1975; Stubbs et al., 2014).

Although the idea of photoemission-led charging is widely accepted as an "averaged picture" of forming positive potentials on the day side, some surface geometric features may open up interesting possibilities for localized, but unconventional scenarios of charging. This aspect is of particular importance for solid natural bodies in space, because numerous variations of surface geometries with different spatial scales can be found. There are plenty of boulders and rocks with various shapes. In smaller scales, regolith particle layers can form wide variety of surface geometries such as bumps and dips. The present study aims to demonstrate that a plasma condition relevant to the solar wind exhibits an ability of locally producing positive potentials by itself, even without photoemission (or any other electron emission processes), when a certain class of surface geometry, a cavity, is considered. The targeted cavity is the one with an opening to the upper space, and thereby precipitating plasma particles are partially accessible to it. Such surface structures in a decameter scale were identified as "vertical holes" or "pits" on the Moon (Haruyama et al., 2009), and its electric environment was examined by means of numerical plasma simulations (Miyake & Nishino, 2015). In smaller scales, complex pileup of small rocks and regolith particles reduces to an irregular surface. Some local geometries of the surface can be categorized into cavities. The electrostatic aspects related to such small cavities have been one of outstanding issues of great interest (Wang et al., 2016; Orger et al., 2019)

The charging processes of irregular surfaces have been investigated via numerical and ground-experimental approaches in efforts to advance electrostatics on the Moon and other small bodies. On their dayside surfaces, the presence of impact craters or boulders gives rise to differential solar UV irradiation and even local shadows. These features lead to non-uniform potential distribution over the surface (e.g., Farrell et al., 2007; Zimmerman et al., 2011; Poppe et al., 2012; Zimmerman et al., 2012; Wang et al., 2019). The shadow can be also regarded as a region of limited access for a solar wind plasma. The plasma expansion theory has been applied to interpret the extent of plasma incursion beyond a shadow boundary (Farrell et al., 2007). Electrostatic structures in even smaller scales, as those of regolith particles, are also of particular interest. In such scales, disability of the Debye shielding leads to more intense electrostatic fields, which is believed as one of important factors for mobilization and breakdown of charged regolith particles (Zimmerman et al., 2016).

We numerically work on electric potential profiles and their associated motions of solar wind plasma particles in the vicinity of a cavity. The model cavity is assumed to have a depth-width aspect ratio ranging from 1 to 6, which is greater than typical values for impact craters. The investigations are focused on loss processes of thermal electrons and ballistic ions within a space bounded by solid sidewalls of the cavity. In such a situation, ions will have a greater residual ratio than electrons, and a current balance condition will be altered significantly at a cavity bottom. We will demonstrate that this feature is feasible, by means of three-dimensional particle-in-cell simulations with plasma conditions relevant to the solar wind (Miyake & Nishino, 2015). As the orthogonal grid system is employed in the simulator in use, we study a rectangular-shaped cavity to exploit its resolution ability. Despite the artificial shape, we will show that physical insight

abstracted from the simulation results can constitute one aspect of charging evolving on natural small bodies. We note that edge effects caused by the shape is also interesting in itself, but are beyond of the scope of the present study.

This study is organized as follows. Section 2 describes the numerical simulation model. The major simulation results are presented and discussed in Section 3. We first focus on the most simplified situation of cavity surface charging by only imposing a solar wind downflow to its surface. The obtained result indicates that positive potentials are formed at the cavity bottom even without any electron emission processes. The electrostatic structure and the associated particle motions are investigated to elucidate the charging mechanism. We subsequently introduce the effects of photoelectron emission and discuss a role of photoelectrons in altering a current balance condition inside the cavity. Section 4 discusses some important aspects for applications of the identified charging mechanism to electrostatics on the Moon and other airless small bodies. Finally, Section 5 concludes with a summary of the main findings and provides perspectives of further studies.

2 Numerical Experiment Setup

Plasma environment near a solid surface with a single cavity is modeled by using an in-house full-particle plasma simulator: EMSES (Miyake & Usui, 2009). The simulation tool is based on the standard electromagnetic particle-in-cell (PIC) method (Birdsall & Langdon, 2018; Hockney & Eastwood, 1981), whereas its basic functionality is designed for addressing plasma interactions with solid inner boundaries. PIC describes a plasma as a bunch of charged macro-particles, each of which represents many real plasma particles. The computational particles are initially distributed over a computational domain except for the interior of solid bodies, and their motions are represented by Newton's equations of motions. Electromagnetic field components are defined discretely on computational grid points. Note that since the present study focuses on electrostatic structures near a solid surface with a cavity, we solve only Poisson's equation for electrostatic potential to compute particle pushing fields. The field and particle datasets are then updated simultaneously by employing the finite difference scheme.

An important feature of EMSES is a capability of incorporating solid objects into computations. The object surfaces are represented as internal boundaries, which satisfy appropriate conditions for both particles and field components. Once a charged particle collides with a solid structure, the particle is regarded as sticking to the surface and no longer processed as a "active particle". EMSES keeps monitoring particle positions to detect sticking particles and eliminate them from a list of active particles. Electric charges carried by colliding particles are deposited onto a surface. Particle emission processes such as photoemission are numerically processed as particle release from a surface. EMSES loads new particles with appropriate positions and velocities complying with the physical processes in consideration.

The computational kernel of EMSES is parallelized with the Message Passing Interface (MPI) based on the block domain decomposition. To avoid possible computational efficiency degradation, EMSES adopts a dynamic load-balancing algorithm referred to as OhHelp, which equalizes per-MPI-process loads in association with both particle and field datasets (Nakashima et al., 2009). Scalable parallel PIC computations regardless of particle distributions are achieved with the benefit of this sophisticated auxiliary algorithm (Miyake & Nakashima, 2013). This aspect is of particular importance in addressing the physics of body-plasma interactions because such phenomena may cause outstanding inhomogeneity of particle distributions.

A box-shaped simulation space is partitioned into spaces occupied by plasma particles and a solid matter, and their interface is configured in such a way that it shapes a plane surface and a single deep depression (i.e., cavity). As the lunar soil is highly re-

sistive (e.g., Olhoeft et al., 1974), the simulated surface is modeled as a perfect insulator. This indicates that electric charges of particles hitting the surface are accumulated in situ. We take the z-axis of the Cartesian coordinates in the direction of elevation. The (plane) surface of the planetary body is then defined as the reference of the z coordinate. The lower limit of the simulation space is located at $z = -30$ m. The total volume of the simulation space is $16 \times 16 \times 128$ m^3. The entire space is discretized with uniform grids of 0.5 m. The square-shaped cavity is assumed to have dimensions of a fixed width $W = 5$ m and a variable depth D ranging 5–20 m. For convenience, we denote the z-coordinate of the cavity bottom as $z_{\rm b}$. A key geometric parameter is the depth-width aspect ratio of the cavity defined as $R_{\rm D/W} = D/W$, which is varied within 1–6 in the present study. Note that the model cavity has a spatial scale comparable to the Debye length $\lambda_{\rm D} \sim 10$ m in the solar wind plasma. Such a cavity may be larger than what can be found typically on natural planetary bodies in space. The size parameters were chosen such that we can exploit the sweet spot of the numerical scheme in terms of available computational resources and spatial resolutions gained by them. Since a target of broader interest would be smaller cavities practically, we later on discuss applicability of the obtained insight to such smaller sizes.

The solar wind plasma is initially distributed in the simulation space and also continuously loaded from its top and lateral edges. The bulk velocity $v_{\rm b}$ and the unperturbed density n_0 of the solar wind are given as 400 km/s and 5 /cc, respectively. We assume that simulated electrons and ions are in an iso-thermal condition, and their temperature is given as 10 eV. The combination of the chosen parameters provide the associated velocity ratio $v_{\rm te} : v_{\rm b} : v_{\rm ti} = 42.9 : 12.9 : 1.0$, where $v_{\rm te}$ and $v_{\rm ti}$ represent the thermal velocities of electrons and ions, respectively. Later on, we will show that the given ordering $v_{\rm te} > v_{\rm b} > v_{\rm ti}$ is another key factor for unconventional charging properties inside the cavity. To elucidate physical processes related to charging, this study carries out simulations with increasing complicating factors in a step-by-step fashion. We first present the results of simulations that intentionally exclude photoemitted electrons. This basic exercise is followed by the results of calculations that take into account the the effects of photoelectrons.

Based on the experimental setup described above, we calculated the charging process of the model cavity until the steady-state solutions were obtained. Figure 1 illustrates a result obtained from the simulation runs, which is highlighted in the present study. The figure displays a three-dimensional view of surface potential for $R_{\rm D/W} = 4$. The representative result clearly shows significant potential enhancement in the innermost part of the cavity. The following section explores an unconventional mechanism underlying in the cavity charging. For reasons of space constraints, the two-dimensional profiles shown hereafter are displayed with the aspect ratio changed from the physical one.

3 Results

3.1 Electrostatic Structure near a Cavity

PIC computations addressed here are focused on the surface charging without any electron emission processes. This aims to clarify effects of a surface shape (i.e., cavity) and a plasma bulk motion on the solar wind plasma inflows to the surface. Although the photoelectron emission is in fact essential in considering dayside surface charging, lessons from the basic investigations will derive a number of key physical features of distinctive charging mode evolved at the cavity surface. This section adopts a fixed cavity aspect ratio $R_{\rm D/W} = 4$, and the dependency on the important parameter is studied in the subsequent section.

Figure 2 shows the spatial profiles of electric potential near the surface for four combinations regarding the presence of a cavity and a bulk flow. Figure 2a displays the po-

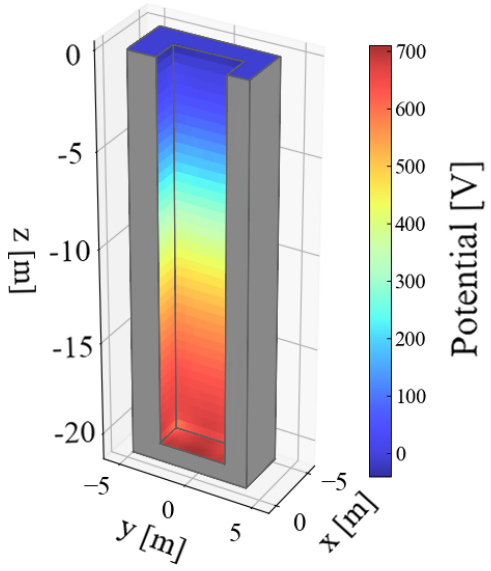

Figure 1. Three-dimensional view of the surface potential distribution obtained from the simulation run with the cavity depth-width aspect ratio $R_{D/W} = 4$. In the simulation, the photoelectron emission is intentionally excluded to clarify an unconventional current ordering between solar wind electrons and ions developed at the cavity bottom.

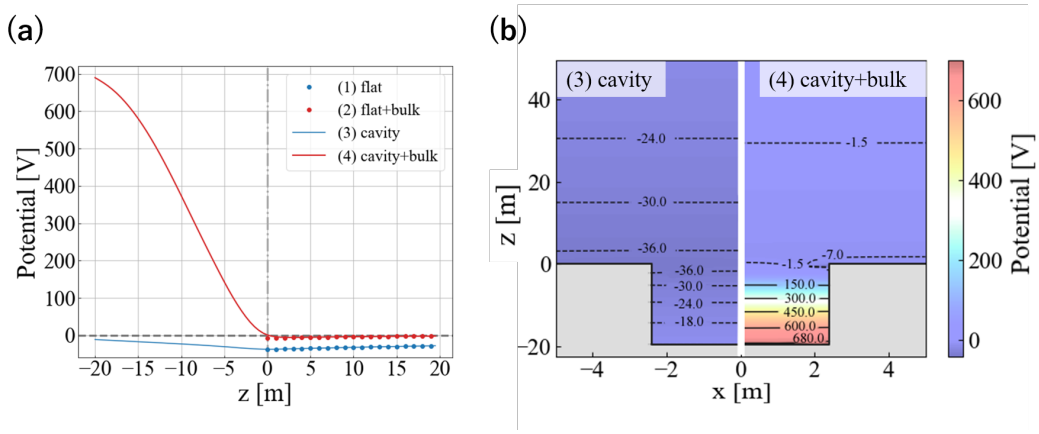

Figure 2. Spatial profiles of an electric potential near the surface for four combinations regarding the presence of a cavity and a bulk flow. The cavity aspect ratio $R_{\mathrm{D/W}} = 4$ is used in the numerical calculations. One-dimensional potentials (a) are plotted along z-axis placed at the center of the cavity. The dotted plots represent potential profiles obtained from simulations without a cavity. Two-dimensional profiles (b) show potential structures in a xz plane cutting the center of the cavity. Note that the panel (b) is displayed not in a physical aspect ratio but in an adjusted ratio $z/x = \sim 10$ for visibility. (See the scales on the vertical and horizontal axes.)

tential distributions along z-axis penetrating the center of the xy plane ($x = y = 0$ m). The ranges $z < 0$ and $z > 0$ correspond to the inside and outside of the cavity, respectively. The potential values at $z = -20$ m correspond to surface potentials at the cavity bottom. For the cases with the cavity, the two-dimensional profiles are also displayed in Figure 2b, the left and right halves of which correspond to the stationary and flowing plasma cases, respectively. All potential values are referenced at $z = \sim 100$ m above the plane surface.

The potential profiles from the simulation without the cavity (the dotted plots in Figure 2a) conform to the classical floating potential theory for a surface in plasma (e.g., Whipple, 1981). Attributed to the higher differential flux for electrons than ions, the surface attains a negative potential such that the current balance between electrons and ions, i.e., $J_\mathrm{i} - J_\mathrm{e} = 0$, is established at each position, where J_i and J_e denote the ion and electron current densities, respectively. With a plasma bulk motion, the surface potential becomes less negative. This is a consequence of increased $J_mathrmi$ while $J_mathrme$ is less affected by the large thermal velocity. Analytical formulations of J_i and J_e estimated surface potentials -8.0 and -38 V for the cases with and without the bulk flow, respectively. The simulations are in reasonable agreement with the estimates, except for a small deviation resulting from the finite size of the simulation domain not being sufficient to cover a long presheath extending above.

The presence of the cavity alters the situation drastically. This is in particular pronounced for the case with the downward plasma bulk motion (i.e., the solid red line in Figure 2a and the right half of Figure 2b). Although the potential near the cavity aperture is comparable to that without the cavity, it continues to increase with depth, eventually reaching +700 V at the cavity bottom. The high potential is not limited to the center of a cavity floor but covers an entire floor as well as sidewalls near the floor, as indicated in the two-dimensional plot. Such extraordinary charging is not identified for the stationary plasma case, even with the cavity; the negative potential relaxes with depth and settles to about -10 V at the bottom.

The outlined result exhibits a number of key features associated with charging of inner-cavity surfaces. One distinctive aspect of the result is the positive potential, which the cavity floor attains in an equilibrium state. This is in contrast to common knowledge that a solid surface in contact with an electron-ion plasma is ordinary floating at a negative potential. The high-degree charging is also an outstanding feature. The potential value +700 V is comparable to the kinetic energy of individual protons +840 eV associated with their bulk motions. Such quantitative association suggests a leading role of an ion bulk motion as a determining factor of an electrostatic energy acquired by the innermost part of the cavity. This speculation is supported by the fact that the case without bulk motion shows no manifestation of such positive charging. To clarify the underlying mechanism of the key result, we next see density and velocity field profiles obtained for the cases with the cavity.

Figure 3 shows the electron and ion density profiles on the plane cutting the center of y-axis, on which the velocity vector field of each species is overlaid with arrows. The left and right halves of each panel correspond to the results for stationary and flowing plasma cases, respectively. The flowing plasma case exhibits a pronounced difference between the ion and electron densities. The electron density declines drastically inside the cavity, whereas the ion density keeps an unperturbed level halfway down the cavity, and even gets enhanced in its innermost part. Reminding the ordering of relevant velocities $v_\mathrm{te} > v_\mathrm{b} > v_\mathrm{ti}$, the density feature is interpreted as consequences of diverging (non-directional) motions of electrons into the solid walls of the cavity, and directional trajectories of ions due to the appreciable bulk velocity. Such an orbit-mechanical picture is supported by the comparison between electron and ion velocity field profiles, indicating more divergent nature of motions for electrons than ions.

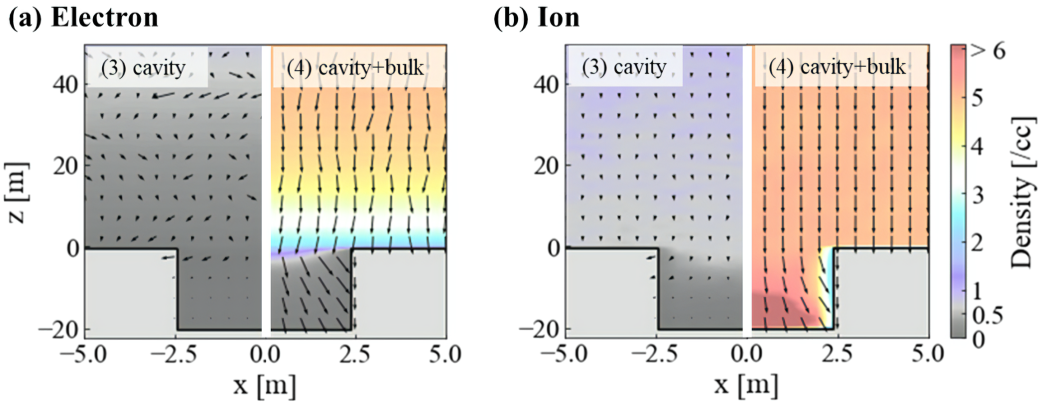

Figure 3. Plasma density and flux vector with a cavity (r_{wh}=4). (a) and (b) Electron and ion density and flux vector with (right) or without (left) the bulk flow, respectively. The vector lengths are proportional to the magnitude (in a logarithmic scale) of the local fluxes.

The distinct difference between ion and electron motions results in much greater sticking rate for electrons than ions at the sidewall boundaries of the cavity. This also implies that the solar wind ions should be more accessible to the bottoms of deep cavities formed on planetary bodies, under the condition that the surface segments are situated within visible fields from the Sun. The condition leads to the reversed ordering of plasma currents, i.e., $J_{\rm i0} > J_{\rm e0}$, where $J_{\rm i0}$ and $J_{\rm e0}$ represent the ion and electron current densities to an uncharged surface. Such unusual current ordering triggers positive charging, even if, in principle, there are no electron emission processes. The potential difference between the aperture and bottom of the cavity can rank with kinetic energy of ion bulk motions, although the potential difference is strongly dependent also on cavity geometries. Associated intense electric field plays an essential role in regaining ion-electron current balance, through repelling some fraction of incoming ions as well as drawing electrons into the cavity floor before they stick to the sidewalls.

Ion-driven charging identified herein is conditioned not only on the presence of a space enclosed by solid walls (like a cavity), but also on an appreciable $v_{\rm b}$ speed exceeding $v_{\rm ti}$ because the velocity ordering $v_{\rm te} > v_{\rm b} > v_{\rm ti}$ is the key to unbalanced sticking rates between electrons and ions at cavity sidewalls. This is evident also from the other simulation with a stationary plasma (Figure 1), in which the density and velocity profiles of ions are less differentiated from those of electrons inside the cavity. With nearly zero or small $v_{\rm b}$, ion motions are less directional like electrons, and are more likely to stick to the sidewall of the cavity. We note that even when considering a stationary plasma, ions near a surface should attain a certain bulk velocity toward the surface due to acceleration within sheath and pre-sheath regions. Such bulk motion energy makes the ions a bit more accessible to the innermost part of the cavity, and results in marginal rise of potential, as outlined in Figure 2a.

3.2 Dependence on a Cavity Aspect Ratio

Given that the aforementioned interpretation for the unconventional charging holds, the bottom potential should have a strong dependence on the depth-width aspect ratio $R_{\rm D/W}$ of the cavity. Figure 4 examines such dependence by plotting potentials measured at the center of the cavity floor, $\phi_{\rm b}$ as a function of $R_{\rm D/W}$. (The condition $R_{\rm D/W} = 0$ corresponds to a case only with a plane surface, i.e., no cavity.) With introducing the cavity and increasing $R_{D/W}$, $\phi_{\rm b}$ turns into positive and rises monotonically up to 800 V.

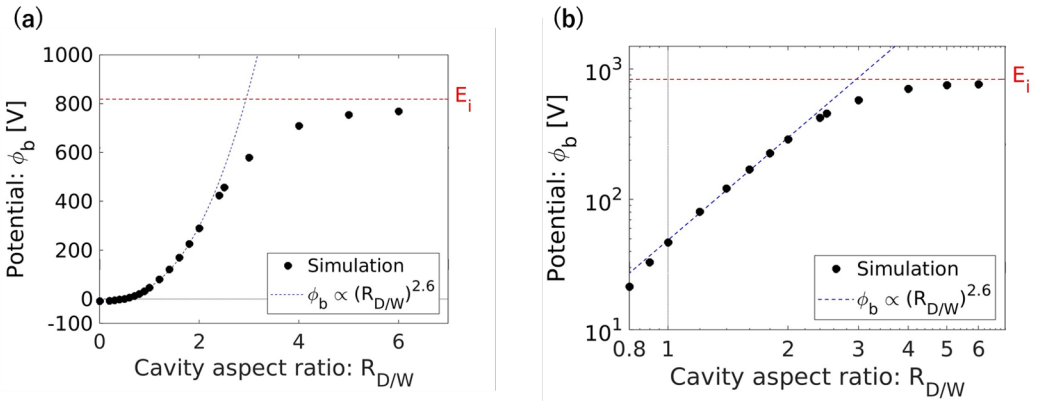

Figure 4. The dependence of the cavity bottom potential on the depth-width aspect ratio. The vertical (potential) axis of the figures is scaled in (a) linear and (b) logarithm. The potential value is measured at the center of the cavity floor.

The trend reflects the fact that the degree of difference between electron and ion motions, in terms of their sticking rates at the sidewall and the resulting accessibility to the bottom, is more pronounced for deeper cavities. The examination also reveals the asymptotic behavior of ϕ_b as a function of $R_{D/W}$. For $R_{D/W} \leq 2$ (referred to as regime I hereinafter), $\phi_b(R_{D/W})$ is found to be the best fit with a power function of $(R_{D/W})^{2.6}$, as confirmed in the double logarithmic plot (Figure 4b). For $R_{D/W} > 2$ (regime II, in the same manner), ϕ_b begins to saturate, and asymptotically approaches a positive potential ~ 800 eV. This potential is comparable to the ion kinetic energy $E_i = 840$ eV for the drift speed $v_b = 400$ km/s. It is insightful to study separately how current balance conditions are established in these two regimes.

As the cavity sidewall causes current imbalance $(J_{i0} - J_{e0})|_{z=-z_b} > 0$ (where the subscript 0 indicates current values for "uncharged" surfaces) at the bottom, the identified charging effect ($\phi_b > 0$) should lead to increasing an electron current (i.e., $J_e > J_{e0}$), decreasing an ion current (i.e., $J_i < J_{i0}$), or both. In the regime II where $\phi_b \sim E_i$, an potential barrier formed inside the cavity is capable of repelling incoming ions. In fact, it has been confirmed in the simulation that some of precipitating ions are electrostatically backscattered upward in this regime. In the regime II, the declination of J_i plays a major role in establishing current balance. This is in contrast to an object in an electron-ion plasma with a negative floating potential, which maintains current balance by repelling electrons.

In the regime I where $\phi_b \ll E_i$, the situation gets a bit more complicated. In this regime, an ion-repulsive force alone is insufficient to recover current balance, because ions, which individually have energies comparable to E_i, are hardly repelled by the forces. Hence, an electron-attractive force must be in charge of current balance by drawing electrons into the cavity. A smaller cavity transit time leads to a lower proportion of electrons sticking to the cavity sidewall, which in turn increases the proportion of electrons attaining the cavity bottom (i.e., $J_e > J_{e0}$). This enhanced J_e may rank with the ion current $J_i \sim J_{i0}$, resulting in the establishment of current balance.

To test this physical scenario, let us consider the "free fall" motion of an electron where the only force acting on it is a vertical (upward) electric field. For further simplicity, we assume that the vertical electric field is spatially uniform, i.e., $E_c = \phi_b/D$. The cavity transit time τ_e, for which the electron reaches the cavity bottom, is expressed as $\tau_e = D\sqrt{2m_e/e\phi_b}$, under an assumption that the initial downward velocity of the

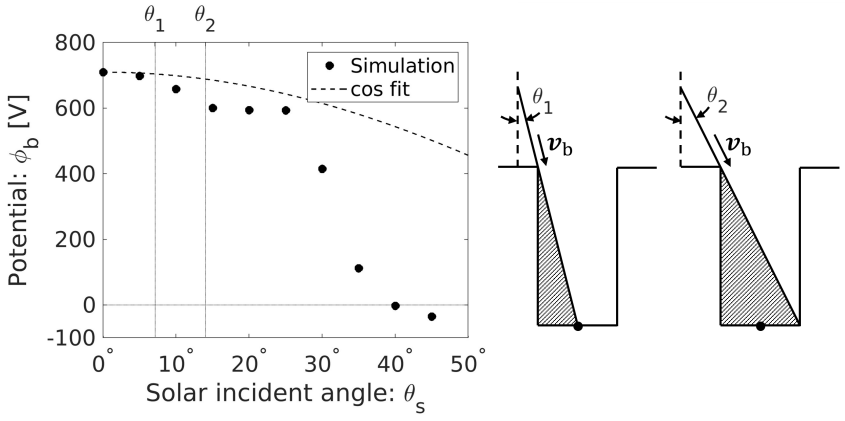

Figure 5. The dependence of the cavity bottom potential on the solar wind incident angle θ. The plotted potential values are the ones measured at the center of the cavity floor.

electron is sufficiently small and negligible compared with its final speed after acceleration. This transit time is used to calculate traversing distances $v_x\tau_e$ and $v_y\tau_e$ in the x and y directions, respectively, for an electron with constant transverse velocities v_x and v_y. Since $|v_x|\tau_e > W/2$ or $|v_y|\tau_e > W/2$ indicates that such electrons are not accessible to the center of the cavity floor, we now obtain the maximum transverse velocities $(v_{x,\max}, v_{y,\max}) = (1/R_{D/W})\sqrt{e\phi_b/8m_e}$ for electrons that are accessible to the center of the floor without being captured by the sidewall. These velocities (i.e., $\pm v_{\{x,y\},\max}$) are used as lower and upper limits of integral range of the velocity distribution function (in v_x–v_y space) to evaluate J_e at the cavity bottom.

As long as the ion current is virtually unchanged by the charging, i.e, $J_i \sim J_{i0}$, in the regime I, its counterpart J_e should be also constant and $J_e \sim J_{i0}$. This indicates that $v_{\{x,y\},\max}$ should be invariant in that regime. It follows that the cavity bottom potential should have a dependence of $\phi_b \propto (R_{D/W})^2$ so that $v_{\{x,y\},\max}$ remains unchanged. While the discussion so far is very simplistic, it is a relatively good representation of the fact that the cavity bottom potential is well characterized by power functions of a dimensionless parameter, i.e., the width-depth aspect ratio $R_{D/W}$ of the cavity. These arguments also provide further evidence that the main physical root of the unconventional charging phenomena presented herein is the shadowing effect by the cavity sidewall, which scrapes off the diagonally incident component of electrons in their velocity space. In the course of the above discussion, we use a number of crude assumptions such as that electrons have zero downward velocity at the inlet of the cavity, which is, of course, not practical. Finite initial downward velocities would enhance J_e and then reduce ϕ_b from the simple estimate discussed above. The deviation would be more pronounced for small $R_{D/W}$ and less so for large $R_{D/W}$ values. This may be the reason behind the simulation results that ϕ_b scales with a greater power (i.e., 2.6) of $R_{D/W}$ than the factor of 2. More rigorous treatments for the assumptions used in the analysis would be available and will be presented in the future studies.

3.3 Solar Wind Irradiation Angle Dependency

Irradiation angle of the solar wind is also an important factor. Figure 5 examines this aspect by showing ϕ_b for solar irradiation angles θ varying through 0° to 45°, in which the cavity aspect ratio remains unchanged as $R_{D/W} = 4$. As θ increases within $0^\circ < \theta < 25^\circ$, ϕ_b declines gradually but remains at several hundreds of volts. The small declination in ϕ_b is attributed to a reduction in the vertical component of a bulk velocity

due to increased inclination of the flow. Reminding that $R_{\mathrm{D/W}} = 4$ is within the regime II, the reduction in kinetic energy of ion vertical motions results in the declination in ϕ_{b}.

The potential decreases sharply for $\theta > 25^{\circ}$ and turns into negative at $\theta > 40°$. It is speculated that the sharp ϕ_{b} declination implies that the cavity floor gets inaccessible to solar wind ions coming at further oblique angles. For $\theta > 30^{\circ}$ we confirmed that an ion flow majorly hits the sidewall of the cavity and cannot reach the cavity bottom, although not shown herein. It should be recognized, however, that the center of the cavity bottom is already in solar eclipse by the sidewall, even at much lower angles such as $\theta = 10^{\circ}$. Thus, maintaining a fairly high ϕ_{b} in $10^{\circ} < \theta < 25^{\circ}$ suggests that ion trajectories are not straight but deflected inside the cavity.

Ion deflection is actually identified in the present simulations. Figure 6a displays ion density and velocity field profiles simulated for $\theta = 20^{\circ}$. The ion flow expands into a shadow region, which enables a fraction of ions to reach the cavity bottom. Several physical processes may be possible to interpret the expansion of ions. The action of an ambipolar electric field is one of possible explanations. In this scenario, ion expansion into the plasma void region is preceded by that of electrons led by pressure gradient forces. It is known that the expansion rate in the case is characterized by an ion acoustic speed. The role of this ambipolar electric field was often referred to as a primary factor in a quasi-neutral plasma expansion into permanently shadow regions on the Moon (e.g., Zimmerman et al., 2011). Note that while the above expansion mechanism is based on the condition that the core plasma is quasi-neutral, the plasma entering the cavity this time is in somewhat a different condition. Since electrons in the cavity are significantly reduced by the sidewall, the quasi-neutral condition is broken and ions behave like an unneutralized beam. The beam divergence mechanism should cause the ions to expand even more efficiently into the shadow region than the ambipolar field effect.

The cavity sidewalls itself also play an important role in guiding incoming ions to the innermost part of the cavity. Due to the oblique solar wind flow, the sunlit sidewall surface is charged a few tens of volts higher than the shadowed sidewall when compared at the same depth from the cavity entrance. The associated horizontal component of the electrostatic field acts to deflect deflects ion trajectories slightly such that their collision with the sunlit sidewall is mitigated to some extent. The deflected ions can penetrate deeper and eventually contribute to the positive charging at the cavity bottom. The "ion-guiding" effect of a thin cavity is also an important aspect for the charging process proposed herein, because it implies that the ion-driven charging is likely to be developed for broader ranges of the solar irradiation angles than what is constrained by geometric configurations.

3.4 Effect of Photoelectron Emission

In the simulations presented thus far, we intentionally excluded the effects of photoelectron emission. In practice, the photoemission is recognized as a leading process for the surface charging in the sunlight (Grobman & Blank, 1969; Stubbs et al., 2014), as a typical photoemission current is in average greater than those of the solar wind as well as the Earth's magnetospheric plasmas. Inside the cavity, however, its role would differ from that commonly known for the charging of flat surfaces. This section discusses how the photoemission affects a current balance and the resultant charging properties. For this purpose, we examined two additional cases with photoemission for the solar irradiation angles $\theta = 0^{\circ}$ and 20°. The major parameters of photoelectrons are as follows; the temperature is $T_{\mathrm{pe}} = 2.2$ eV and the current density is $J_{\mathrm{pe}} = 4.5\ \mu\mathrm{A/m}^2$ for normal solar incidence. Actual photoelectron yield at each sunlit location is scaled as $\cos\theta$, depending on the local solar incidence θ. For simplicity, the photoelectron energy distribution is assumed to be a simple Maxwellian, and their angular distribution

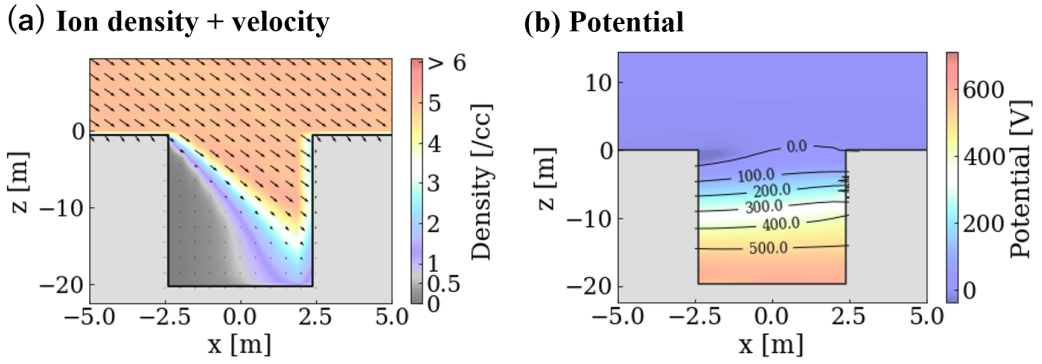

Figure 6. Two-dimensional profiles of (a) ion density and flux vector and (b) potential in case of an oblique solar wind incidence ($\theta = 20^{\circ}$). The vector lengths are proportional to the magnitude (in a logarithmic scale) of the local fluxes.

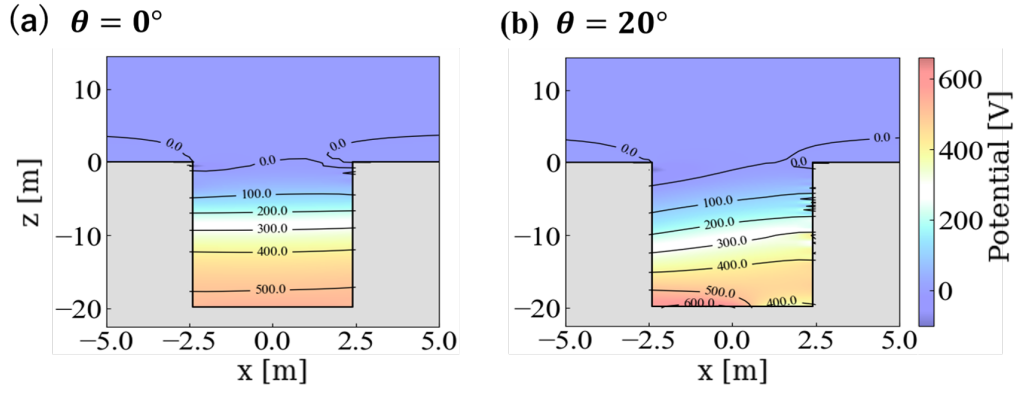

Figure 7. Two-dimensional potential profiles obtained from the simulations with photoelectron emission for (a) $\theta = 0^{\circ}$ and (b) 20°.

of emission shall follow a cosine function. The cavity aspect ratio $R_{\mathrm{D/W}} = 4$ was used in the numerical experiments.

Figure 7 shows the potential profiles near the cavity. For $\theta = 0^{\circ}$, the plane and cavity bottom surfaces release photoelectrons, whereas the cavity sidewall does not. The surface potential outside the cavity is at a few volts positive and comparable to the photoelectron temperature, which is consistent with previous estimates of dayside surface potentials (Poppe & Horanyi, 2010). The photoelectron escaping current, which is restrained by the positive potential, is balanced with the solar wind electron inflow. In contrast, the potential structure inside the cavity remains similar to that obtained without photoemission. This result suggests that the function of electrons photoemitted in the depths of the cavity is limited. Owing to the reversed ordering of the solar wind current components $(I_{\mathrm{i}0} - I_{\mathrm{e}0})|_{z=-z_b} > 0$, negative excess charges need to be brought to the cavity bottom to establish a current balance there. The photoelectron release is, in principle, unable to take on this role because it tends to deposit positive charges to the surface and further lift up its positive potential. In fact, the cavity bottom potential is much greater than the photoelectron temperature, and thereby virtually all photoelectrons emitted at the cavity bottom are recollected immediately. This implies that the photoelectrons emitted in situ have limited impact on the potential structure near the cavity bottom.

The role of photoelectrons in charging the inner surface of the cavity is manifested in a different manner. We demonstrate this in the simulation for $\theta = 20^{\circ}$ (Fig. 7b), in which (a part of) the sidewall surface in turn releases photoelectrons, but the bottom does not. The left half of the cavity floor still maintains a rather high potential ($> +600$ V), whereas the potential of the right half is relaxed to a few hundreds of volts. The partial relaxation of the positive potential at the cavity bottom is clearly caused by electrons photoemitted by the sidewall. The ion-driven cavity charging process generates an intense upward electric field inside the cavity. The electric field leads some of photoemitted electrons into the innermost part of the cavity. Such photoelectrons compensate for the build-up of excess positive charges at the cavity bottom due to ion bombardment.

The identified feature brings to light the important aspect of photoelectrons acting as negative charge carriers, which can move from a certain sunlit location to another (not necessarily sunlit) location on solid surfaces. This is clearly distinguished from the commonly quoted effect of photoelectrons for the charging in sunlight: i.e., the process that transfers negative charges from the surface to space. The photoelectron ability to relax the differential charging is highly dependent on the surface topography of an area exposed to sunlight, as inferred from the comparison between the two different conditions for the solar irradiation angle. This also indicates the importance of the cavity geometry itself. Specifically, the proportion of a sunlit area in the sidewall seems to be one of crucial factors in the effect. Further testing on practical cavity geometries will potentially elucidate this important aspect.

4 Discussion

Although a cavity targeted in this study is limited to that with a specific geometry, the obtained results provide some clues to generalization of the revealed charging process. The significant positive charging directly reflects the directionality difference between electron and ion motions, which gets pronounced when the velocity ordering $v_{\mathrm{te}} > v_{\mathrm{b}} > v_{\mathrm{ti}}$ holds. Under the condition, electrons and ions would exhibit unbalanced penetrability against the cavity. This can lead to the strong differential charging between upper and deep areas of the cavity surface.

Similar charging processes have been recognized and investigated in the field of the plasma processing. During plasma etching of a typical dielectric structure such as a trench,

the differential charging arises between upper and bottom parts of the structure (Arnold & Sawin, 1991; Kinoshita et al., 1996; Hwang & Giapis, 1997; Ishchuk et al., 2012; Memos & Kokkoris, 2016). The effect has been a subject of ongoing investigations (Memos & Kokkoris, 2016; Zhang, 2021) because the resulting electric field (or the potential difference of tens of volts) possibly causes some anomalies in the finish of the etching process. In this case also, differential features of electron and ion motions have been referred to as the root cause of the anomalous charging process. The present study demonstrates the analogy of physical processes emerging in these different application fields, in the light of electric charging of rough surfaces. We also note a difference between the two situations in that the kinetic energy of ions originates from the solar wind flow in the present study, while that is acceleration within the sheath in the plasma etching case. This distinction is directly related to the resultant magnitude of potentials developed in the two situations.

We here discuss a few important aspects that have not been addressed so far, although the detailed analysis on them is beyond the scope of the present study. One important aspect is the spatial scale of a cavity. The present numerical study considers a cavity of a few tens of meters on its long side, which can be encountered rarely in nature. Thus a question that inevitably arises is how the charging condition will be for smaller cavities. One clue to this point is in the fundamental charging mechanism derived from the parametric study, which is described in Section 3.2. The physical root of the highly-positive potential is electron depletion at the innermost part of a deep cavity, which is caused by shadowing of electrons by the sidewalls. This shadowing effect should be in principle governed by a dimensionless parameter, i.e., the aspect ratio, rather than the size itself of the cavity. Furthermore, rather small, sub-Debye-scale cavities are considered to better fit this simple scaling law, as particle trajectories get less influenced by space charges inside the cavity. In view of the rough discussion, it is reasonable to assume that the ion-driven charging works also for small cavities.

Given that the upper limit of a cavity bottom potential is constrained by ion kinetic energies, the solar wind speed is one of key parameters for the charging process. Although the present study employs a representative value of 400 km/s, the speed is subject to change depending on solar activity conditions. It is well known that the bulk velocity can approach 600–800 km/s in fast solar wind stream conditions. Such conditions would give rise to further significant charging exceeding a few kV positive at the bottom surfaces of deep cavities. In practice, the cavity potential will be determined in combination with other physical parameters such as the electron temperature as well as processes such as the charge relaxation by photoelectrons, both of which do play roles that cannot be ignored. The dependence on such conditions need to be surveyed comprehensively in the future works.

Possible contribution to mobilizations of small dust grains covering planetary bodies is another important aspect. The distinctive feature of the derived charging effect is that surface patches with positive charges are lying in the depths of the cavity, and thereby their potential fields are hidden from upper space. Such localized potential difference may lead to an intense electrostatic field, which suggests possible implications for some sort of dust grain mobilizations. We should note that the present study does not conclude that the identified charging effect works exclusively on dust mobilizations in an electrostatic sense. It is reasonable to consider that the effect coexists with other charging modes such as proposed by Wang et al. (2016) inside the cavity, depending on a lighting condition of each surface patch. A critical implication from the series of studies is that solid surfaces with irregular geometries can produce irregular potential distributions even in sub-Debye scales. This also leads to the importance of investigating possible effects of the associated localized electric fields in the context of possible drivers of dust mobilizations. Since such investigations should suffer from an issue of numerous degrees of free-

dom regarding the structural features of cavities, not only deterministic simulations as addressed herein but also some statistical approaches would be necessitated.

5 Conclusions

The charging properties of a surface with a deep cavity are numerically studied with plasma conditions relevant to the solar wind. The investigations were conducted with applications to possible irregularities on the surface of solid planetary bodies in mind, although specific shape and size are employed in the simulations. The PIC computations predict the formation of positive potentials that reach a few to several hundreds of volts at the cavity bottom. In forming such unconventional charging state, incoming ions do play a lead role as positive charge carriers from space to the depths of the cavity. This is also supported by the parametric analysis indicating that the upper limit of the potentials is bounded by the kinetic energy of ions moving with a solar wind flow speed. Electron access to the cavity bottom is restricted to a considerable degree due to their much higher sticking rate to the sidewall compared with the ions. In this sense, the identified feature can be also regarded as one form of boundary-driven charging processes, in which the solid boundary exclusively shadows thermal electrons. The present study also identifies the creepage motions of photoelectrons as a major relaxation factor against the intense charging inside the cavity. The key finding is that photoelectrons emitted from the sidewall, not from the bottom of the cavity, take this role. Based on this, the geometric configurations of the cavity itself and locations of the area irradiated by sunlight are inferred to be a crucial factor in determining the relaxation efficiency. To summarize, we have numerically demonstrated the unconventional fashion of surface charging in space, which may contribute to storage and release of electrostatic energies at the irregular surfaces of solid planetary bodies.

A critical issue at present is the lack of observational or experimental data that provide evidence of the physical process proposed herein. A significant feature of the present results is in the fact that the potential field itself is lying in the depths of the cavity structures and hidden from the upper space. Nevertheless, an intense electric field within the cavity potentially has an ability to accelerate positive charged particles upward. Thus remote observations of reflected ions or lofted dust grains coming from a surface with cavities and their correlations with environmental conditions may help providing evidence for the proposed scenario. Further numerical experiments should also be considered to develop generalized physical models of the charging process itself as well as its effects on charged particle transport. In particular, the scaling behavior of the charging process with respect to cavity size needs to be addressed to clarify its applicability to sub-Debye scale cavities.

Acknowledgments

The present study was supported in part by the Japan Society for the Promotion of Science: JSPS (Grant No. 20K04041), the innovative High-Performance Computing Infrastructure: HPCI (Project No. HP210159), and the Joint Usage/Research Center for Interdisciplinary Large-scale Information Infrastructures: JHPCN (Project No. JH210047) in Japan. The computations in the present study were performed using the KDK system at the Research Institute for Sustainable Humanosphere (RISH), Kyoto University, the supercomputer system at the Information Initiative Center, Hokkaido University, and the ITO system at the Research Institute for Information Technology, Kyushu University, Japan. The authors would like to thank Hideyuki Usui at Kobe University, Japan for fruitful discussions on the numerical results. Y. Miyake would like to extend his deepest appreciation to Hiroshi Nakashima, who passed away in 2021, for his long-term support on the use of state-of-the-art HPC technologies.

Open Research

Data Availability Statement

The simulation data needed to reproduce the presented findings are available in the Zenodo open-access repository (https://doi.org/10.5281/zenodo.7033350).

References

Arnold, J. C., & Sawin, H. H. (1991). Charging of pattern features during plasma-etching. *J. Appl. Phys.*, *70*(10), 5314-5317. doi: 10.1063/1.350241.

Birdsall, C. K., & Langdon, A. B. (2018). *Plasma Physics via Computer Simulation.* CRC press.

Fahleson, U. (1967). Theory of electric field measurements conducted in magnetosphere with electric probes. *Space Sci. Rev.*, *7*(2-3), 238-262. doi: 10.1007/Bf00215600.

Farrell, W. M., Stubbs, T. J., Halekas, J. S., Killen, R. M., Delory, G. T., Collier, M. R., & Vondrak, R. R. (2010). Anticipated electrical environment within permanently shadowed lunar craters. *J. Geophys. Res. Planets*, *115*. doi: 10.1029/2009je003464.

Farrell, W. M., Stubbs, T. J., Vondrak, R. R., Delory, G. T., & Halekas, J. S. (2007). Complex electric fields near the lunar terminator: the near-surface wake and accelerated dust. *Geophys. Res. Lett.*, *34*(14), 1-5. doi: 10.1029/2007GL029312.

Freeman, J. W., & Ibrahim, M. (1975). Lunar electric-fields, surface-potential and associated plasma sheaths. *Moon*, *14*(1), 103-114. doi: 10.1007/Bf00562976.

Garrett, H. B. (1981). The charging of spacecraft surfaces. *Rev. Geophysics*, *19*(4), 577-616. doi: 10.1029/RG019i004p00577.

Garrett, H. B., & Whittlesey, A. C. (2000). Spacecraft charging, an update. *IEEE Trans. Plasma Sci.*, *28*(6), 2017-2028. doi: 10.1109/27.902229.

Grobman, W. D., & Blank, J. L. (1969). Electrostatic potential distribution of sunlit lunar surface. *J. Geophys. Res.*, *74*(16), 3943-+. doi: DOI10.1029/JA074i016p03943.

Halekas, J. S., Delory, G. T., Lin, R. P., Stubbs, T. J., & Farrell, W. M. (2008). Lunar prospector observations of the electrostatic potential of the lunar surface and its response to incident currents. *J. Geophys. Res. Space Physics*, *113*(A9). doi: 10.1029/2008ja013194.

Halekas, J. S., Mitchell, D. L., Lin, R. P., Hood, L. L., Acuna, M. H., & Binder, A. B. (2002). Evidence for negative charging of the lunar surface in shadow. *Geophys. Res. Lett.*, *29*(10). doi: 10.1029/2001gl014428.

Haruyama, J., Hioki, K., Shirao, M., Morota, T., Hiesinger, H., van der Bogert, C. H., ... Pieters, C. M. (2009). Possible lunar lava tube skylight observed by selene cameras. *Geophys. Res. Lett.*, *36*. doi: 10.1029/2009gl040635.

Hockney, R. W., & Eastwood, J. W. (1981). *Computer Simulation Using Particles.* Taylor & Francis, Inc.

Hwang, G. S., & Giapis, K. P. (1997). On the origin of the notching effect during etching in uniform high density plasmas. *J. Vacuum Sci. Tech. B*, *15*(1), 70-87. doi: 10.1116/1.589258.

Ishchuk, V., Volland, B. E., Hauguth, M., Cooke, M., & Rangelow, I. W. (2012). Charging effect simulation model used in simulations of plasma etching of silicon. *J. Appl. Phys.*, *112*(8). doi: 10.1063/1.4759005.

Kinoshita, T., Hane, M., & McVittie, J. P. (1996). Notching as an example of charging in uniform high density plasmas. *J. Vacuum Sci. Tech. B*, *14*(1), 560-565. doi: 10.1116/1.588431.

Manka, R. H. (1973). Plasma and potential at the lunar surface. In R. J. L. Grard (Ed.), *Photon and Particle Interactions with Surfaces in Space* (p. 347-361).

Springer Netherlands.

Memos, G., & Kokkoris, G. (2016). Modeling of charging on unconventional surface morphologies of pmma substrates during ar plasma etching. *Plasma Processes and Polymers*, *13*(5), 565-578. doi: 10.1002/ppap.201500176.

Miyake, Y., & Nakashima, H. (2013). Low-cost load balancing for parallel particle-in-cell simulations with thick overlapping layers. *2013 12th IEEE International Conference on Trust, Security and Privacy in Computing and Communications*, 1107-1114. doi: 10.1109/TrustCom.2013.134.

Miyake, Y., & Nishino, M. N. (2015). Electrostatic environment near lunar vertical hole: 3d plasma particle simulations. *Icarus*, *260*, 301-307. doi: 10.1016/j.icarus.2015.07.011.

Miyake, Y., & Usui, H. (2009). New electromagnetic particle simulation code for the analysis of spacecraft-plasma interactions. *Phys. Plasmas*, *16*(6), 062904. doi: 10.1063/1.3147922.

Nakashima, H., Miyake, Y., Usui, H., & Omura, Y. (2009). Ohhelp: a scalable domain-decomposing dynamic load balancing for particle-in-cell simulations. , 90-99. doi: 10.1145/1542275.1542293.

Nitter, T., Havnes, O., & Melandso, F. (1998). Levitation and dynamics of charged dust in the photoelectron sheath above surfaces in space. *J. Geophys. Res. Space Phys.*, *103*(A4), 6605-6620. (Zf972 Times Cited:116 Cited References Count:53) doi: Doi10.1029/97ja03523.

Olhoeft, G. R., Frisillo, A. L., & Strangway, D. W. (1974). Electrical properties of lunar soil sample 15301,38. *J. Geophys. Res.*, *79*(11), 1599-1604. doi: DOI10.1029/JB079i011p01599.

Orger, N. C., Toyoda, K., Masui, H., & Cho, M. G. (2019). Experimental investigation on silica dust lofting due to charging within micro-cavities and surface electric field in the vacuum chamber. *Adv. Space Res.*, *63*(10), 3270-3288. doi: 10.1016/j.asr.2019.01.045.

Poppe, A., & Horanyi, M. (2010). Simulations of the photoelectron sheath and dust levitation on the lunar surface. *J. Geophys. Res. Space Physics*, *115*. doi: 10.1029/2010ja015286.

Poppe, A., Piquette, M., Likhanskii, A., & Horanyi, M. (2012). The effect of surface topography on the lunar photoelectron sheath and electrostatic dust transport. *Icarus*, *221*(1), 135-146. doi: 10.1016/j.icarus.2012.07.018.

Robertson, S. (2013). Sheaths in laboratory and space plasmas. *Plasma Phys. Controlled Fusion*, *55*(9). doi: 10.1088/0741-3335/55/9/093001.

Scheiner, B., Baalrud, S. D., Yee, B. T., Hopkins, M. M., & Barnat, E. V. (2015). Theory of the electron sheath and presheath. *Phys. Plasmas*, *22*(12). doi: 10.1063/1.4939024.

Stubbs, T. J., Farrell, W. M., Halekas, J. S., Burchill, J. K., Collier, M. R., Zimmerman, M. I., ... Pfaff, R. E. (2014). Dependence of lunar surface charging on solar wind plasma conditions and solar irradiation. *Planet. Space Sci.*, *90*, 10-27. doi: 10.1016/j.pss.2013.07.008.

Stubbs, T. J., HalekaS, J. S., Farrell, W. M., & Vondrak, R. R. (2007). Lunar surface charging: a global perspective using lunar prospector data. *Workshop on Dust in Planetary Systems*, *643*, 181-+.

Stubbs, T. J., Vondrak, R. R., & Farrell, W. M. (2007). A dynamic fountain model for dust in the lunar exosphere. *Workshop on Dust in Planetary Systems*, *643*, 185-+.

Wang, X., Robertson, S., & Horanyi, M. (2019). Plasma sheath formation at craters on airless bodies. *J. Geophys. Res. Space Physics*, *124*(6), 4188-4193. doi: 10.1029/2018ja026235.

Wang, X., Schwan, J., Hsu, H. W., Grun, E., & Horanyi, M. (2016). Dust charging and transport on airless planetary bodies. *Geophys. Res. Lett.*, *43*(12), 6103-6110. doi: 10.1002/2016gl069491.

Whipple, E. C. (1981). Potentials of surfaces in space [Journal Article]. *Reports on Progress in Physics*, *44*(11), 1197-1250. doi: 10.1088/0034-4885/44/11/002.

Zhang, P. (2021). Study on the influence of ion incident energy on surface charging in plasma etching. *Physica Scripta*, *96*(12). doi: 10.1088/1402-4896/ac233e.

Zimmerman, M. I., Farrell, W. M., Hartzell, C. M., Wang, X., Horanyi, M., Hurley, D. M., & Hibbitts, K. (2016). Grain-scale supercharging and breakdown on airless regoliths. *J. Geophys. Res. Planets*, *121*(10), 2150-2165. doi: 10.1002/2016je005049.

Zimmerman, M. I., Farrell, W. M., & Poppe, A. R. (2014). Grid-free 2d plasma simulations of the complex interaction between the solar wind and small, near-earth asteroids. *Icarus*, *238*, 77-85. doi: 10.1016/j.icarus.2014.02.029.

Zimmerman, M. I., Farrell, W. M., Stubbs, T. J., Halekas, J. S., & Jackson, T. L. (2011). Solar wind access to lunar polar craters: feedback between surface charging and plasma expansion. *Geophys. Res. Lett.*, *38*. doi: 10.1029/2011gl048880.

Zimmerman, M. I., Jackson, T. L., Farrell, W. M., & Stubbs, T. J. (2012). Plasma wake simulations and object charging in a shadowed lunar crater during a solar storm. *J. Geophys. Res. Planets*, *117*. doi: 10.1029/2012je004094.

Figure 1.

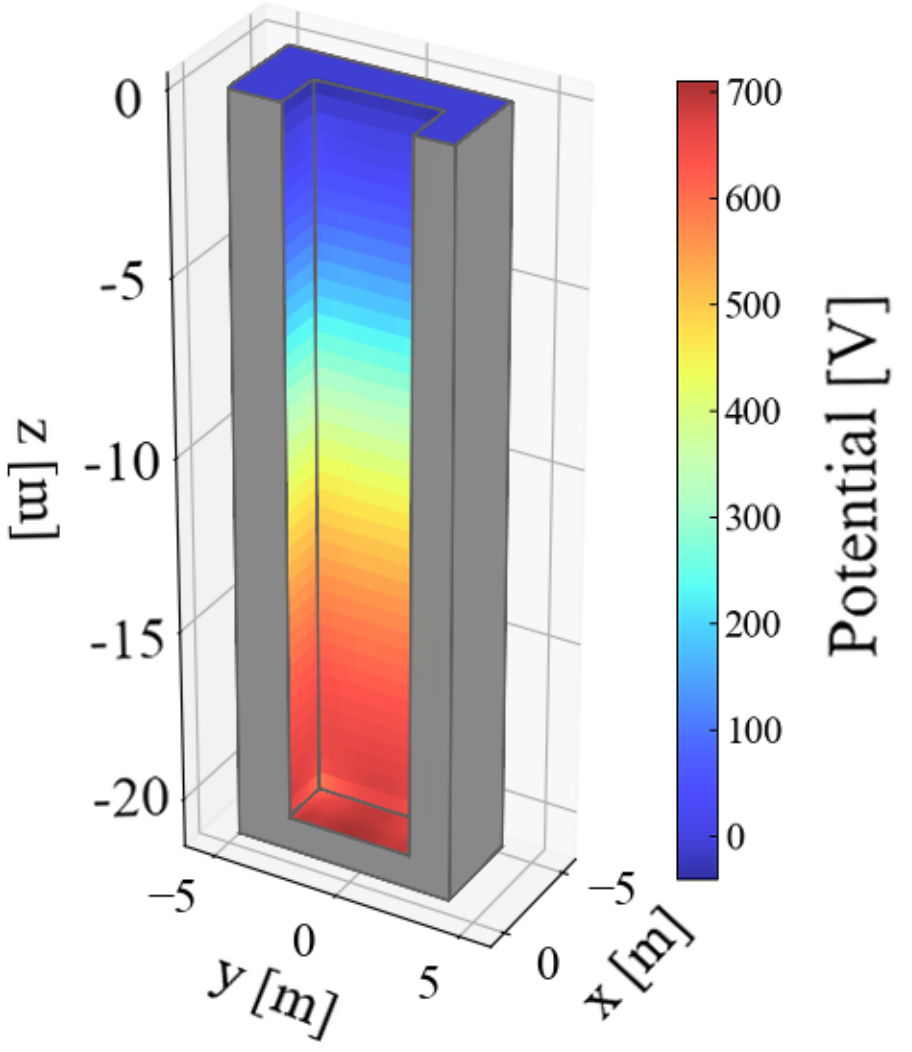
0
-5
-10
-15
-20
[m] z
−5
0
5
y [m]
−5
0
x [m]
700
600
500
400
300
200
100
0
Potential [V]

Figure 2.

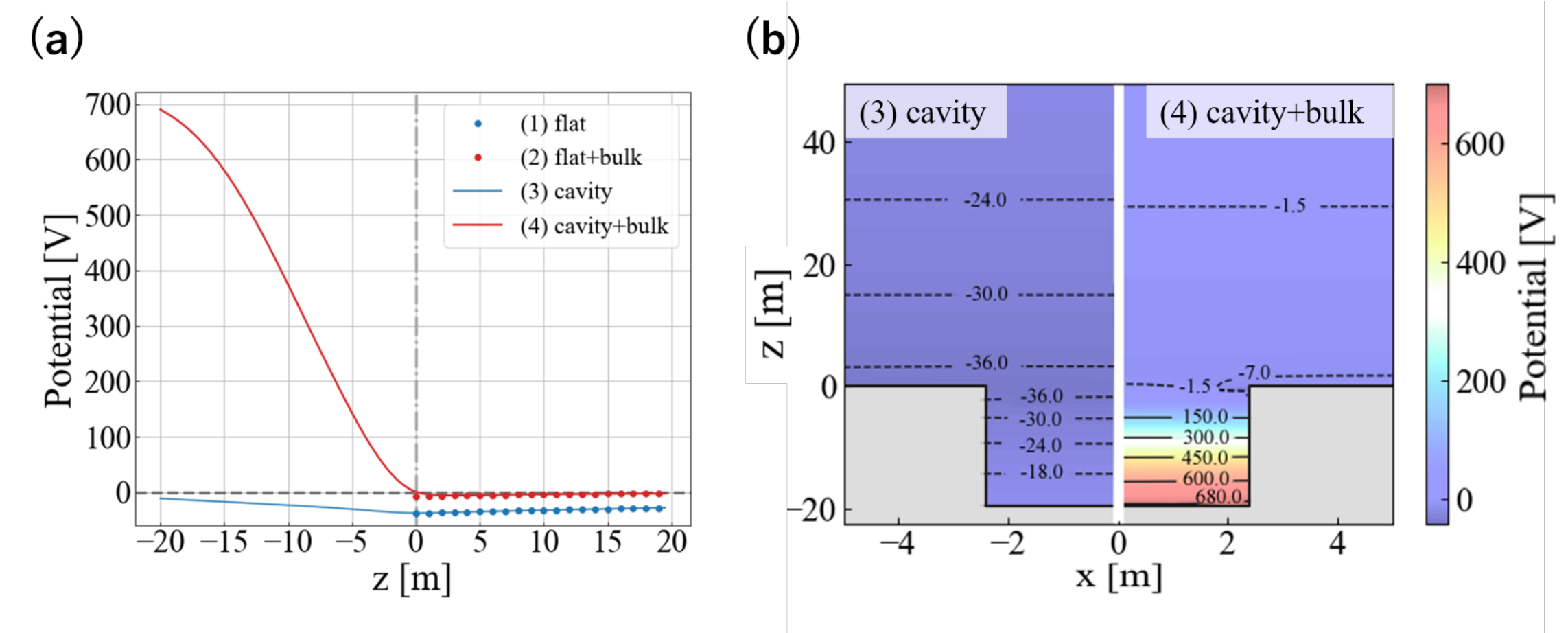
(a)
Potential [V]
z [m]
(1) flat
(2) flat+bulk
(3) cavity
(4) cavity+bulk
(b)
(3) cavity
(4) cavity+bulk
z [m]
x [m]
Potential [V]
-24.0
-30.0
-36.0
-1.5
-7.0
150.0
300.0
450.0
600.0
680.0
-18.0

Figure 3.

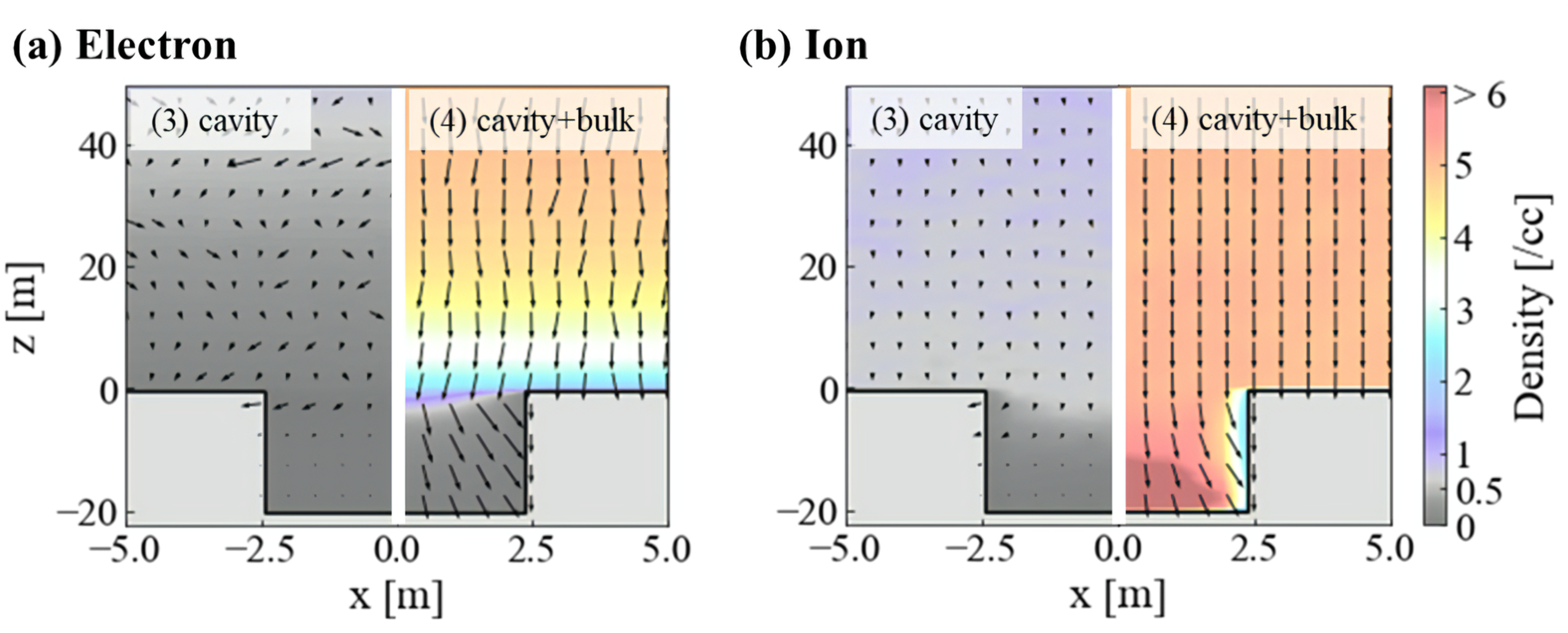
(a) Electron
(b) Ion
(3) cavity
(4) cavity+bulk
(3) cavity
(4) cavity+bulk
z [m]
x [m]
x [m]
40
20
0
−20
−5.0
−2.5
0.0
2.5
5.0
> 6
5
4
3
2
1
0.5
0
Density [/cc]

Figure 4.

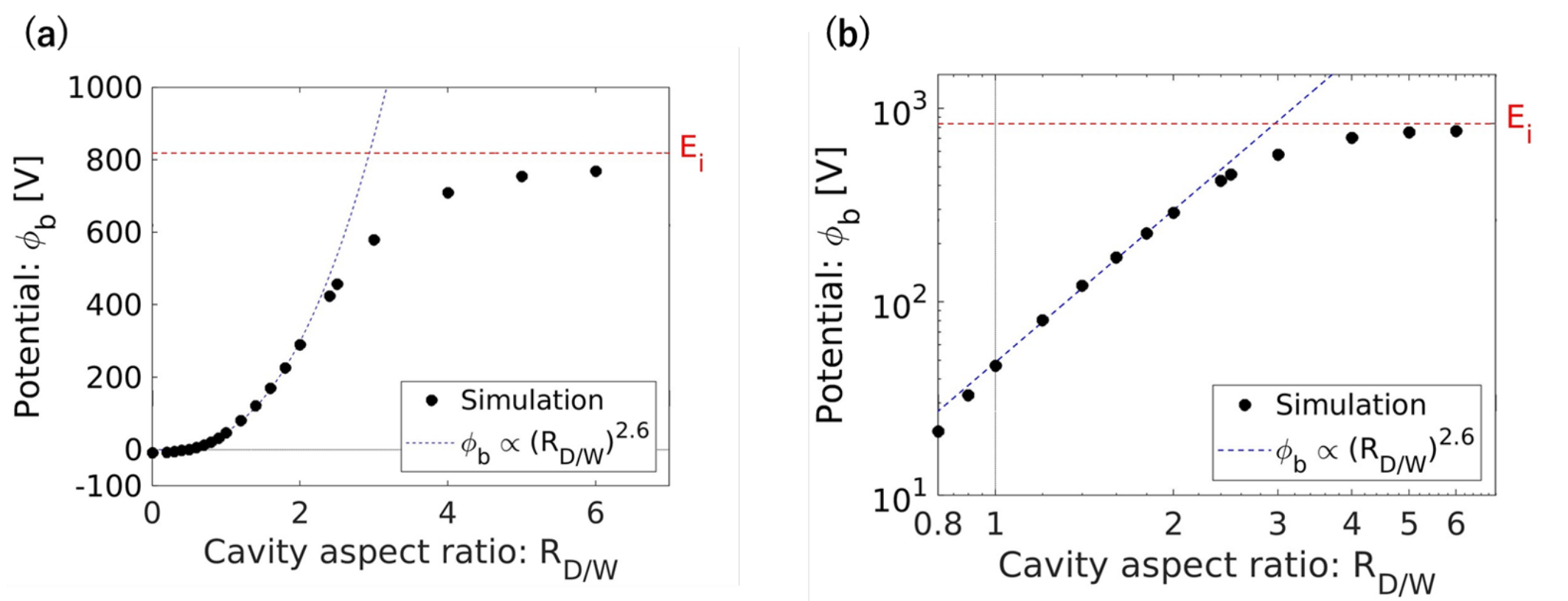
(a)
1000
800
600
400
200
0
-100
0
2
4
6
Potential: ϕ_b [V]
Cavity aspect ratio: $R_{D/W}$
E_i
Simulation
$\phi_b \propto (R_{D/W})^{2.6}$
(b)
10^3
10^2
10^1
0.8
1
2
3
4
5
6
Potential: ϕ_b [V]
Cavity aspect ratio: $R_{D/W}$
E_i
Simulation
$\phi_b \propto (R_{D/W})^{2.6}$

Figure 5.

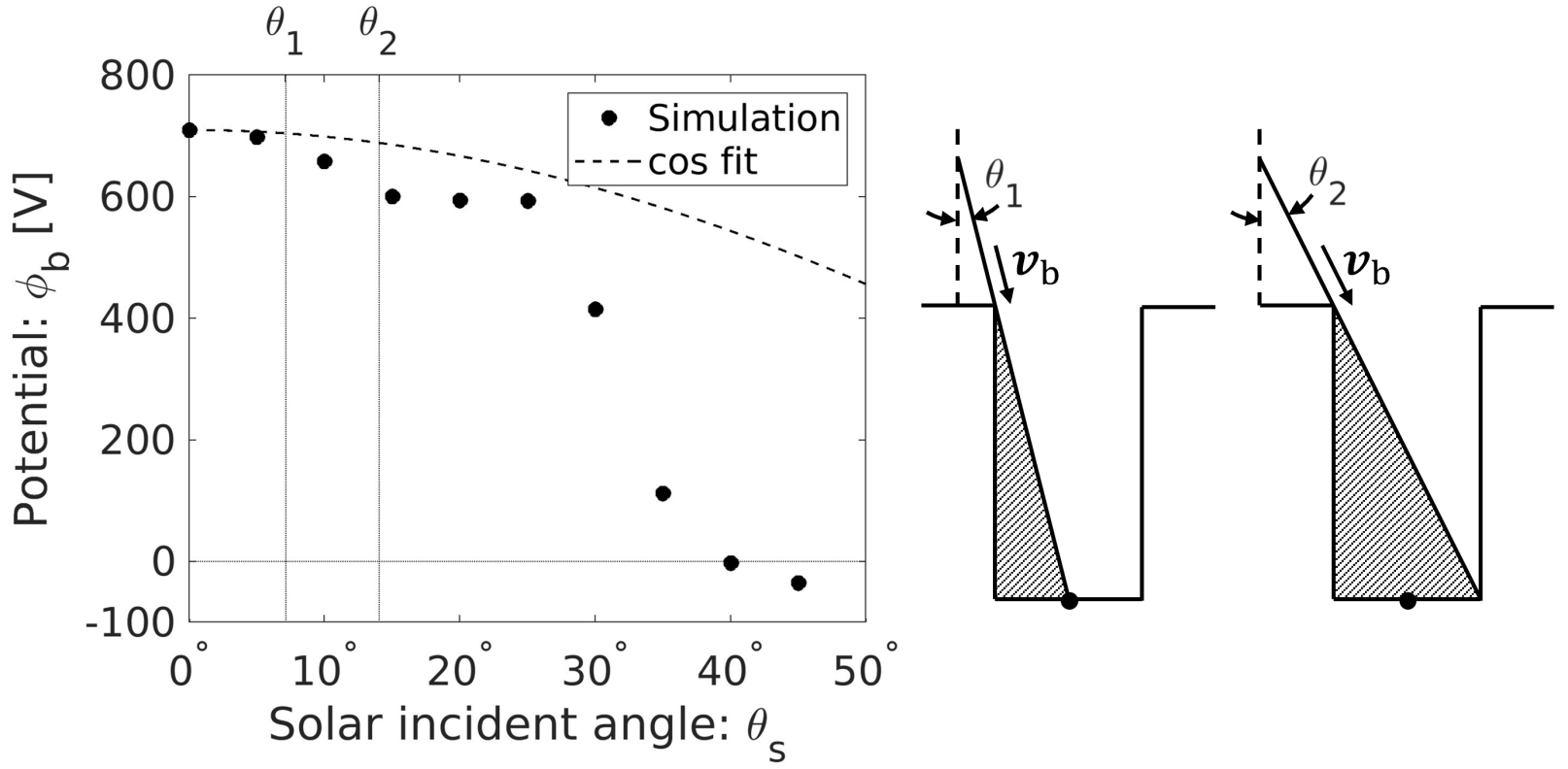
θ_1
θ_2
800
600
400
200
0
-100
Potential: ϕ_b [V]
Simulation
cos fit
0°
10°
20°
30°
40°
50°
Solar incident angle: θ_s
θ_1
v_b
θ_2
v_b

Figure 6.

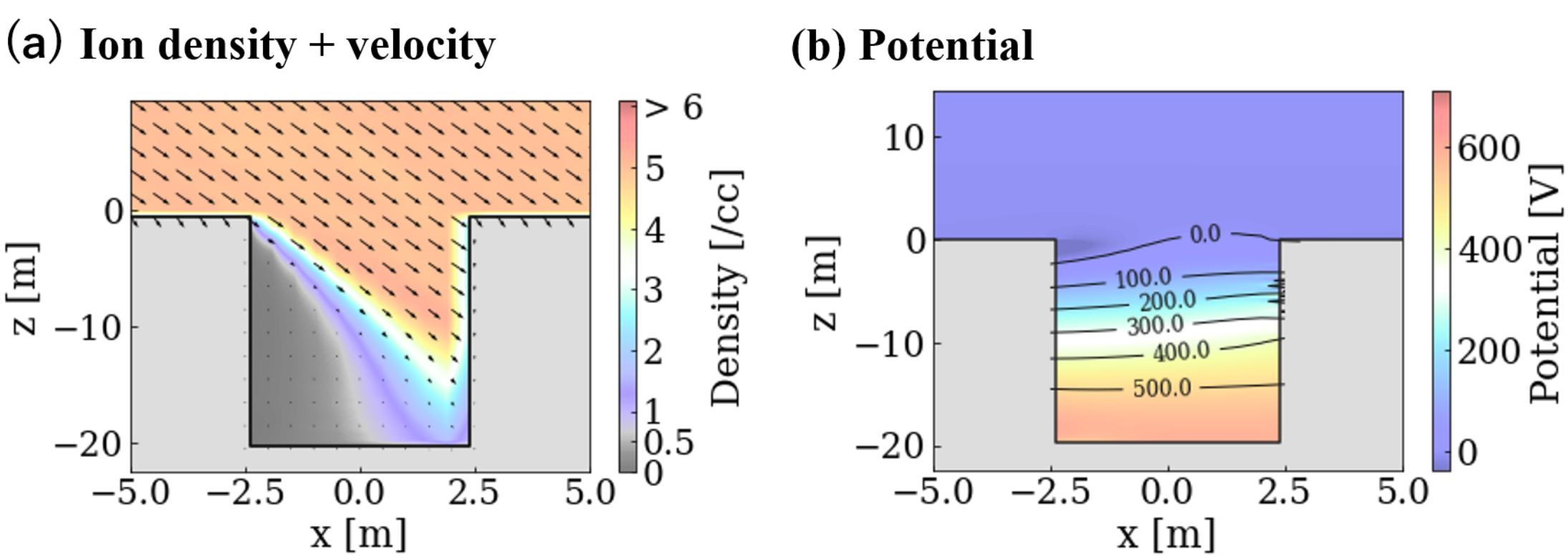
(a) Ion density + velocity
(b) Potential
z [m]
x [m]
Density [/cc]
Potential [V]
0.0
100.0
200.0
300.0
400.0
500.0

Figure 7.

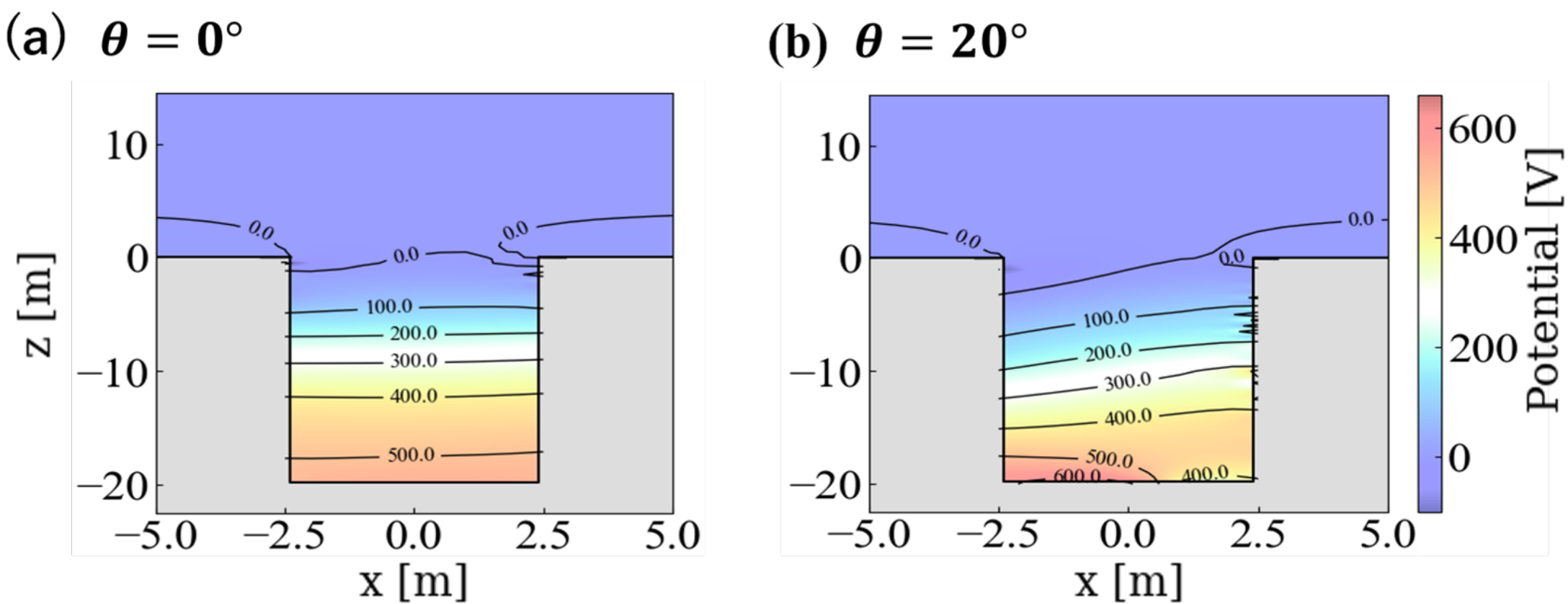
(a) θ = 0°
(b) θ = 20°
z [m]
x [m]
Potential [V]
10
0
−10
−20
−5.0
−2.5
0.0
2.5
5.0
600
400
200
0
0.0
100.0
200.0
300.0
400.0
500.0